Energy & Buildings 222 (2020) 110110

Contents lists available at ScienceDirect

Energy & Buildings

journal homepage: www.elsevier.com/locate/enb

Energy-saving potential of 3D printed concrete building with integrated living wall

Yawen He [a], Yamei Zhang [b,c], Chao Zhang [b], Hongyu Zhou [a,*]

[a] Department of Civil and Environmental Engineering, University of Tennessee, Knoxville TN37996, USA
[b] Jiangsu Key Laboratory of Construction Materials, School of Material Science and Engineering, Southeast University, Nanjing 211189, China
[c] Nanjing Institute for Green Intelligent Additive Manufacturing Co. Ltd, Nanjing 210000, China

ARTICLE INFO

Article history:
Received 2 March 2020
Revised 26 April 2020
Accepted 28 April 2020
Available online 5 May 2020

Keywords:
Digital construction and 3D printing
Green wall
Thermal network model
Thermal comfort

ABSTRACT

Large-scale concrete 3D printing and digital construction has brought enormous potential to expand the design space of building components (e.g., building envelope) for the integration of multiple architectural functionalities including energy saving. In this research, a modular 3D printed vertical concrete green wall system – namely the 3D-VtGW, was developed. The 3D-VtGW envelope was assembled with prefabricated (3D printed) multifunctional wall modular elements, which serves as the enclosure of the building as well as the backbone for a green wall system to improve building's energy efficiency. Using this design concept and large-scale concrete 3D printing, a prototype commercial building was built in Nanjing, China. To quantify the energy-saving potential of the 3D-VtGW system, a thermal network model was developed to simulate the thermal behavior of buildings with 3D-VtGW system and for thermal comfort analysis. Whole-building energy simulation was carried out using Chinese Standard Weather Data (CSWD) of Nanjing, China. The simulation results indicate that the building with 3D-VtGW exhibited prominent potential for energy saving and improved thermal comfort. The integrated greenery system in 3D-VtGW largely reduces wall exterior surface temperature and through-wall heat flux via the combined effects of plant shading, evapotranspiration, and heat storage from soil. This study presents the immense opportunities brought by digital fabrication and construction to extend the design space and function integration in buildings.

1. Introduction

Provoked by recent advancements in additive manufacturing, 3D printable concrete has been explored as an alternative method to construct concrete structures [1–3]. This new construction approach has the potential to address several major challenges in current concrete industry: it eliminates the use of temporary formwork and vibrations that are typically necessary for consolidating wet concrete. This can in turn significantly reduce the material and labor costs involved in the formwork construction; the highly automated construction process can reduce resource demands, greenhouse gas (GHG) emissions, material waste, cut down construction time, and reduce human error [4,5]. In addition, it allows a new approach for concrete design – the material and component can be parametrically designed tuning to the optimal structural performance and functionalities. While numerous research efforts are still underway in various areas including properties of 3D printable cementitious materials [6] – mechanical and rheological properties [7–9], material design optimization [10,11], as well as behaviors of the 3D printed elements[6], including reinforcement strategies for 3D printed concrete structures [12]. Concrete 3D printing technologies including extrusion-based and powder-bedding (e.g. D-shape) printing processes [13], robotics [14–16], and 3D printing of cementitious material under special environment such as underwater [17] and space constructions [18] are also investigated. Besides the research in laboratories, over the last decade, some large-scale applications and showcase examples have become available – e.g. office building in Dubai by Winsun, the interior of a hotel suite by Total Kustom [19] and residential house by Apis Cor [13].

One of the most striking features of 3D printing of concrete (or any other building materials) is the ability to produce architectural components with complex 3D geometry for lower cost in comparison with traditional casting processes [5], hence pushing the boundaries of the design space available for architects and engineers. With large-scale 3D printing technology, unprecedented

* Corresponding author at: 851 Neyland Drive, 417 John D. Tickle Building, Knoxville, TN 37996-2313, USA.

E-mail address: hzhou8@utk.edu (H. Zhou).

https://doi.org/10.1016/j.enbuild.2020.110110
0378-7788/

Nomenclature

A	Area [m^2]
c_p	Specific heat [J/K/kg]
C	Heat capacity of node [J/K]
e	Actual vapor pressure [Pa]
e_s	Saturation vapor pressure of air [Pa]
E	Heat from energy source [J]
F	View factor [–]
G	Heat absorbed by soil [W/m^2]
H	Heat transfer coefficient [W/K]
$I{\downarrow}_s$	Solar radiation incident [W/m^2]
LAI	Leaf area index [–]
LPD	Long-term Percentage of Dissatisfied [–]
m	Mass [kg]
PMV	Predicted mean vote [–]
PPD	Predicted percentage of dissatisfied [–]
q	Heat flux [W/m^2]
Q	Heat rate [W]
r_a	Aerodynamic resistance [s/m]
r_s	Bulk surface resistance [s/m]
R	Thermal resistance [(K·m^2)/W]
R_n	Net radiation at foliage surface [W/m^2]
SHGC	Solar heat gain coefficient [–]
t	Time [s]
T	Temperature [°C]
U	Thermal transmittance [W/(m^2·K)]
V	Differential control volume or finite control volume [m^3]
W	Water mass [kg]
WWR	Window-to-wall ratio [–]

Greek symbols

α	Solar absorptivity [–]
$\beta_{i,f}$	Foliage coverage ratio of surface for node i [–]
γ	Psychrometric constant [Pa/°C]
Δ	Slope of the saturation vapor pressure–temperature curve [Pa/°C]
ε	Surface emissivity [–]
θ_i	Fraction of surface area in the whole layer for node i [–]
λ	Heat conductivity [W/(m·K)]
ρ	Density [kg/m^3]
σ	Stephan-Boltzmann constant [W/(m^2·K^4)]
τ	Surface reflectivity [–]
φ	Repartition coefficient [–]

Subscripts and superscripts

a	Air
abs	Thermodynamic temperature
af	Near-canopy air for foliage
air_ex	Outdoor air
as	Canopy air near soil
f	Foliage layer
grd	Ground (long-wave radiation)
lat	Latent heat
lw	Long-wave radiation
s	Soil layer
sky	Sky (long-wave radiation)
sw	Short-wave radiation
w	Wall layer

level of structural efficiencies and/or multifunctionality through geometry can now be achieved [20] – i.e., additional functions can be embedded in the structural parts, the architectural components are not only constructed for mechanical properties but also serve other functions such as soundproofing and thermal insulation. One of the most loud-speaking examples is the Additive Manufacturing Integrated Energy (AMIE) project initiated by Oak Ridge National Laboratory (ORNL) and Skidmore, Owings & Merrill LLP (SOM) [21] – i.e., the 3D printed AMIE C-shape modular exterior wall explores the potential to condense multiple functions into an integrated shell. AMIE's organic geometries are optimized to reduce localized stress and mitigate turbulent exterior airflow; while the panels' interior ribs are designed to host ultra-high-efficiency atmospherically insulated panels which forms an efficient energy-conserving enclosure. Another example is the building retrofit project developed by Gosselin et al. [16] where the building retrofitting element served as exterior supporting walls for an existing building – the 3D printed elements were designed as absorptive formworks to be filled either with ultra-high performance fiber-reinforced concrete for structural parts or with an insulating material for thermal insulation. Multi-objective optimization was conducted to minimize thermal bridging whilst maintaining its structural performance.

While building energy-saving features have been integrated into the design of 3D printed architectural elements [14,20,22–24], there has not been a systematic study on the energy saving potential of 3D printed concrete buildings. One of the most convenient and easy-to-implement strategies for 3D printed concrete buildings are the integration of passive energy-saving features as such green roof [25–27] and vertical greenery systems (VGS) [28–31]. VGS, often referred to as green façades and living wall systems, are considered as one of the most viable greenery options for buildings since they do not occupy additional space and they can be easily integrated into most new constructions as well as existing building projects [32,33]. Recent studies have indicated that in addition to their aesthetic benefits, VGS also help to improve air quality, reduce noise level, enhance building thermal performance, and minimize heat island effects [34–37]. When compared with green roofs, green walls have larger potential surface area for greening. Thus, VGS has significant potential to contribute to the insertion of vegetation in the urban context without occupying extra space at street level. At the building scale, green walls can reduce the energy demands of buildings by the combined effects of additional insulation provided by the greenery together with the shading for building surfaces and the cooling effects on the surrounding surfaces and canopy air [38].

In this research, the versatile geometry design enabled by concrete 3D printing was leveraged to seamlessly integrate vertical living wall system into a building's exterior enclosure to create a 3D printed concrete green wall system (i.e., 3D-VtGW), see Fig. 1. The 3D-VtGW building was assembled with prefabricated (3D printed) multifunctional wall modules, which serve as the backbone for green wall system to improve building's energy efficiency. To quantify energy-saving potential of the 3D-VtGW system, a thermal network model was developed to simulate energy behavior and thermal comfort of buildings with 3D-VtGW system. Whole-building energy simulations were carried out using Chinese Standard Weather Data (CSWD) of Nanjing, China. This study represents an example demonstrating the extended design space for multifunctional building envelopes enabled by digital construction technique, which allows integration of multiple architectural functions (e.g., energy-saving, acoustic).

2. Configuration of the 3D printed building with 3D-VtGW

The prototype building is located at Jiangbei Kechuang Stadium, Nanjing, China. It has a steel frame structure enclosed with the 3D

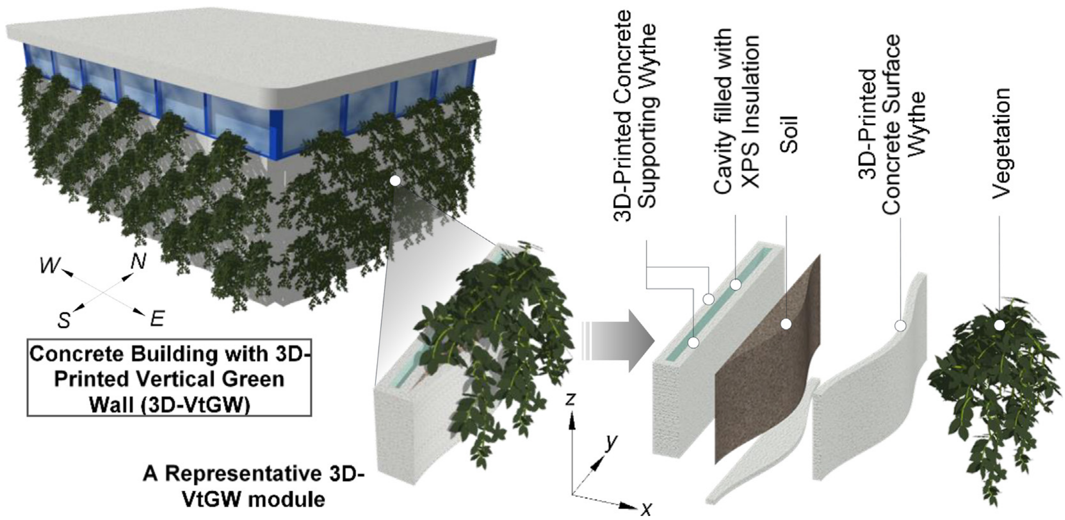

Fig. 1. Building with 3D-Printed Vertical Green Wall (3D-VtGW) and configuration of 3D-VtGW module.

printed vertical green wall system (3D-VtGW). 3D-VtGW is a living wall system assembled with 3D printed modular elements that can serve as the backbone for growing vertical greenery (Fig. 1). As aforementioned, one of the most attractive features of concrete 3D printing of concrete is its ability to produce building components with highly complex 3D geometry and less cost/time as compared to traditional casting process. 3D printing offers technical advantage of reconciliating non-standard shapes to achieve additional architectural functions (other than load-bearing and space separation) such as aesthetics and building energy-saving features. In this study, each 3D-VtGW module is comprised of double-layer supporting wythes as well as a wave-shaped surface wythe to grow greenery, as shown in Fig. 1. The cavity between the two supporting wythes can either be filled with reinforcements (e.g., rebar) and high performance concrete (e.g., UHPC) for load bearing, or thermal insulation foams to improve the building's energy performance. In addition, sinusoidal-shaped exterior surface wythe is integrally printed with the wall module such that the space enclosed by sinusoidal-shaped wythe and the supporting wythes can be filled with soil to grow greenery. The moist soil and vegetation serve as heat sink and shield against solar radiation. In combination with evapotranspiration within the 3D-VtGW module, the integrated living wall will significantly reduce through-wall heat flux and save building energy use during summer months. It is also worth noting that, the designed 3D-VtGW system mostly harvests rain water and building's greywater for irrigation, aiming to achieve easy-to-maintain system with low maintenance cost.

As illustrated in Fig. 2 (a), the 3D-VtGW prototype building was constructed through on-site assembly of prefabricated (3D printed) concrete modules. For the 3D printing process of 3D-VtGW module, a low-critical shear stress mortar premix with only fine aggregates was prepared with a rheological behavior appropriate for pumping and extrusion-based printing. The mortar ink was kept in a shearing mixer to avoid setting before it was conveyed towards a screw-driving extrusion printing head using a peristaltic pump. Then, the preprinted and cured 3D-VtGW modular elements were assembled on-site around a load-bearing steel frame. The joints were grouted with a non-shrinkage cementitious-based sealant to prevent water intrusion and minimize air infiltration. After erecting the roof and placing fenestration components such as windows and door frames, the envelope was painted with the water-proofing surface paint. Lastly, soil with growing vegetation was placed into each green wall module after the installation of irrigation system. Fig. 2 (b) shows pictures of the completed 3D-VtGW buildings at Jiangbei Kechuang Stadium before the vertical greenery was placed. Through a combination of concrete 3D printing technology and modular assembling, the prototype building was complete in less than 30 days, from component production (3D printing) to construction completion.

3. Model formation for the building with 3D printed vertical green wall

The plant in 3D-VtGW is a living component of the building envelope that responds to the environment in a very complicated way [39]. The simulation of heterogenous vertical green wall response is generally not included in commercially available softwares for transient thermal simulation of buildings, making the simulation and design difficult for architects and building designers. In order to study the energy saving potential and thermal comfort performance of buildings with the 3D-VtGW envelope, a hydro-thermal network model was established to perform energy analysis of the heterogeneous building envelope.

In this research, the vertical greenery is represented by three types of node: a node to represent the foliage layer shown in Fig. 3, which captures the sensible heat exchanges, i.e. the short and long-wave radiation balance with the environment and the sky, and convection between the greenery and the surrounding air, the latent heat expelled by the plant transpiration; a second node for the canopy air, where the convective heat balance with outdoor air, foliage, and with the surrounding environment is computed; and another node representing the exterior surface layer of the 3D printed concrete wall which exchanges heat with the two previous nodes through long-wave radiation and convection and also receives a portion of the incoming radiation, and transmits heat to the internal wall node [37]. Similarly, the horizontal greenery is also represented by three types of nodes representing foliage layer, canopy air and soil, where the latent heat exchange brought by evapotranspiration is incorporated in the model. Similar to other existing models for VGS [37], the hydro-thermal network model developed herein is based on a finite difference approach, considering only one-dimensional heat transfer without internal transverse fluxes. The details on the calculation of the evapotranspiration, heat balance, moisture balance and thermal comfort are discussed in the subsequent section.

The indoor space heat exchange considers energy balance of indoor air and interior wall surfaces, including the convective heat

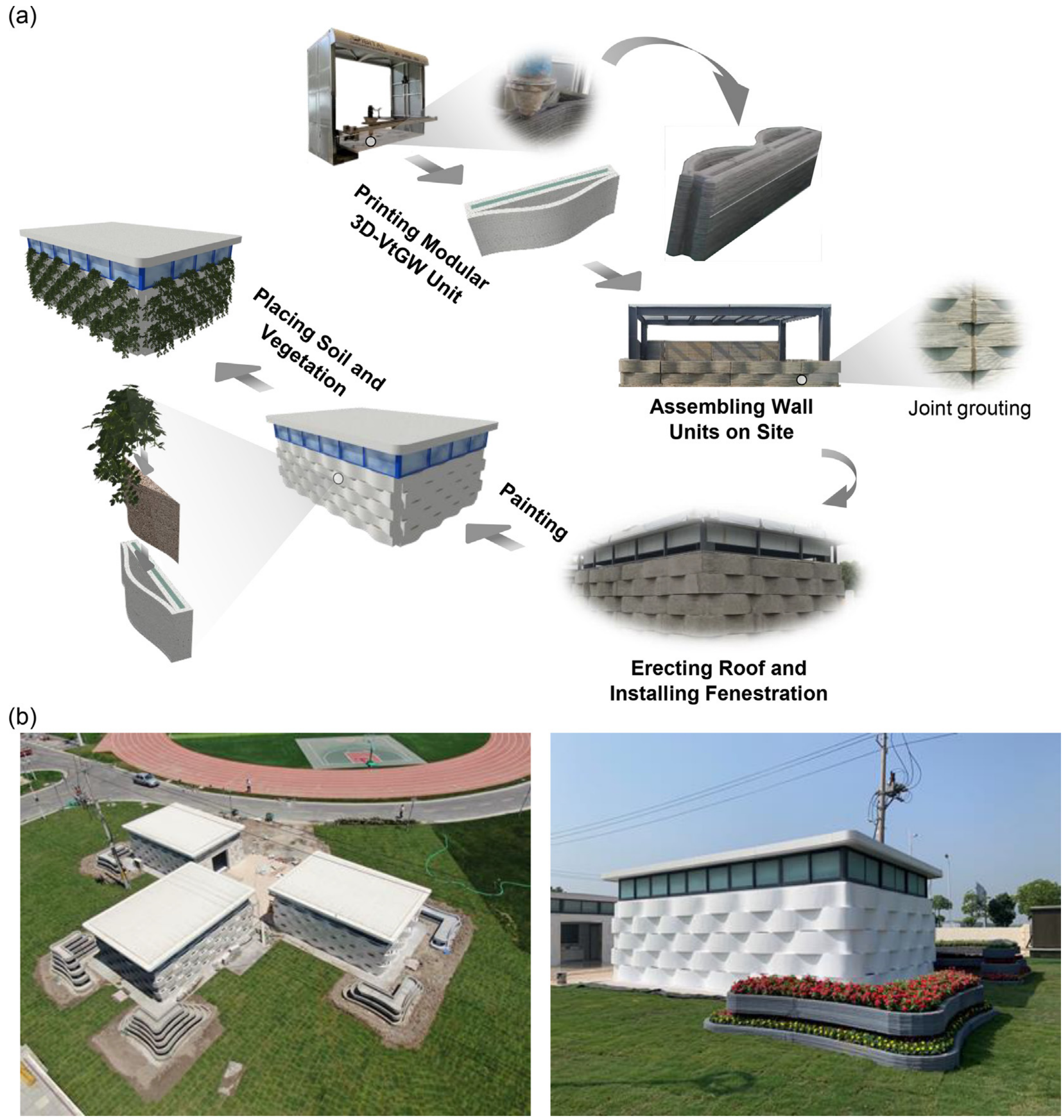

Fig. 2. (a) Schematic showing the construction process of the 3D-VtGW building; and (b) pictures showing the completed prototype buildings.

transfer on interior wall surfaces, long-wave and short-wave radiations from internal sources including human activity, lighting and equipment, as well as the thermal flow from air conditioner and infiltration. The short-wave and long-wave radiations transmitted through glazing, long-wave radiant interaction amongst interior wall surfaces and the glazing are also considered, see Fig. 4 (a) and (b).

3.1. Model formulation for 3D-VtGW

3.1.1. Heat conduction through the heterogeneous 3D-VtGW module

The heat diffusion equation for any point P with temperature $T(x, y, z)$ in a 3D-VtGW module can be expressed as:

$$c_p(x,y,z)\rho(x,y,z)\frac{\partial T}{\partial t} = \left[\frac{\partial}{\partial x}\left(\lambda_x\frac{\partial T}{\partial x}\right)+\frac{\partial}{\partial y}\left(\lambda_y\frac{\partial T}{\partial y}\right)+\frac{\partial}{\partial z}\left(\lambda_z\frac{\partial T}{\partial z}\right)\right] + Q'''_V(x,y,z) \tag{1}$$

where t is time; c_p, ρ, and λ are the material's specific heat, density, and thermal conductivity, respectively; and $Q'''_V(x,y,z)$ is the rate of heat transferred from energy sources (e.g., solar radiant energy, latent heat).

For a differential control volume, Equation (2) is expressed as:

$$\int_V c_p(x,y,z)\rho(x,y,z)\frac{\partial T}{\partial t}dV = \int_V \left[\frac{\partial}{\partial x}\left(\lambda_x\frac{\partial T}{\partial x}\right)+\frac{\partial}{\partial y}\left(\lambda_y\frac{\partial T}{\partial y}\right)+\frac{\partial}{\partial z}\left(\lambda_z\frac{\partial T}{\partial z}\right)\right]dV + \dot{E}_V \tag{2}$$

where V is volume and E_V is the rate of heat transferred from energy sources in this differential control volume.

As aforementioned, each 3D-VtGW module is discretized into a number of finite volumes, as shown in Fig. 3 (a), where the energy balance method [40] is applied. Thus, Equation (2) can be rewritten as a general form for node i in a thermal network as:

$$\int_{V_i} c_p(x_i,y_i,z_i)\rho(x_i,y_i,z_i)dV_i\frac{\partial T_i}{\partial t} = H_i^{i-1}T_{i-1} + H_i^{i+1}T_{i+1} - \left(H_i^{i-1}+H_i^{i+1}\right)T_i + Q_i \tag{3}$$

where subscript i represents the node number; H_i^{i-1} is the heat transfer coefficient representing conduction between node i-1 and

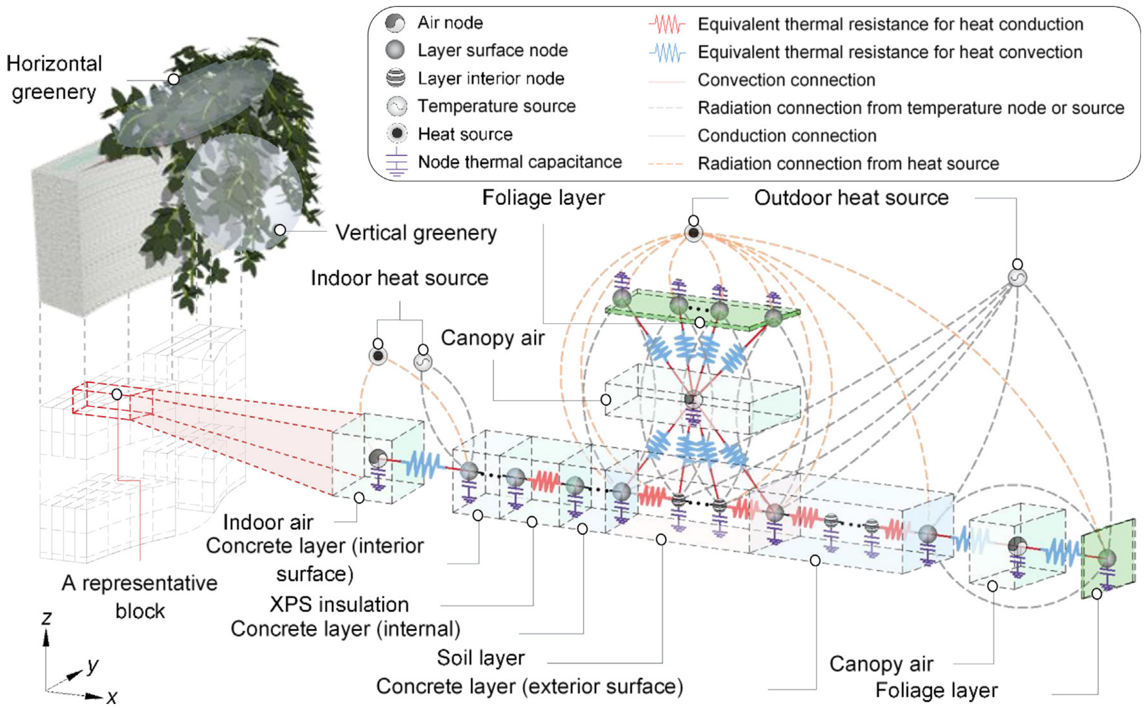

Fig. 3. Nodal network for one representative meshed block along thickness extracted from a 3D-VtGW module.

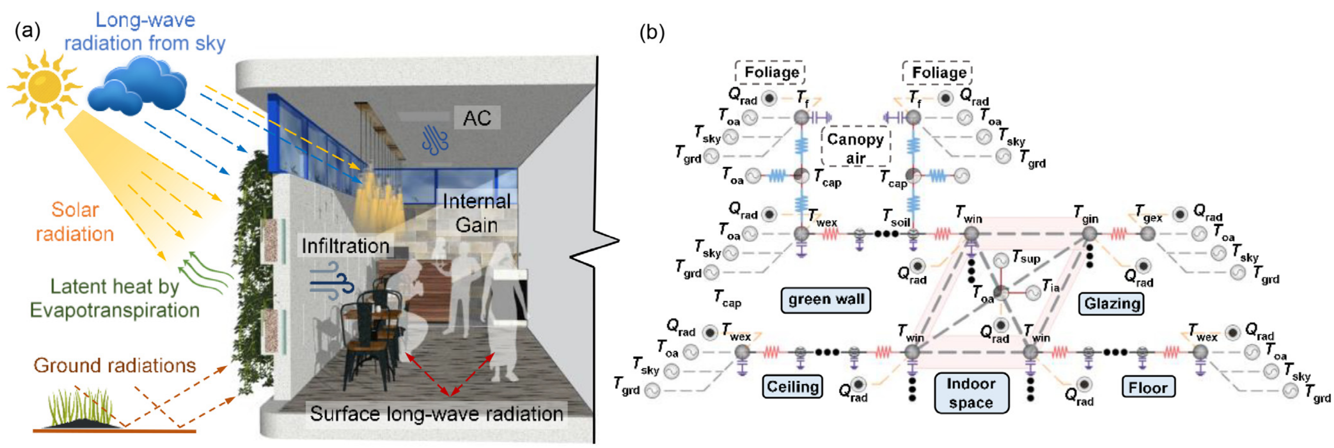

Fig. 4. Schematic showing heat transfer process of the building with 3D-VtGW: (a) schematic of the outdoor and indoor heat sources; and (b) general nodal schematic for a building with living wall system.

node i; Q_i is the rate of heat transfer from energy sources in the finite volume of node i.

3.1.2. Heat balance within foliage

The heat transfer process of plant foliage includes convective heat exchange with ambient air, short-wave radiation ($Q_{i,sw,f}$), long-wave radiation ($Q_{i,lw,f}$) [41] and latent heat from evapotranspiration ($Q_{i,lat,f}$). Thus, equation (3) for the foliage node can be written as:

$$\int_{V_{i,f}} \rho_f(x_i, y_i, z_i) c_{p,f}(x_i, y_i, z_i) dV_{i,f} \frac{dT_{i,f}}{dt} = H_{i,f}^{af}(T_{af} - T_{i,f}) + Q_{i,sw,f} + Q_{i,lw,f} + Q_{i,lat,f} \tag{4-a}$$

$$Q_{i,sw,f} = (1 - \tau_{i,f}) I_s^{\downarrow} A_{i,f} \tag{4-b}$$

$$\begin{aligned} Q_{i,lw,f} = & \left[F_i^{sky}\left(T_{sky,abs}^4 - T_{i,abs,f}^4\right) + F_i^{grd}\left(T_{grd,abs}^4 - T_{i,abs,f}^4\right) \right. \\ & \left. + F_i^{air\_ex}\left(T_{air\_ex,abs}^4 - T_{i,abs,f}^4\right)\right] \\ & \cdot \sigma \varepsilon_{i,f} A_{i,f} + \sum_k \sigma \theta_{i,f} \beta_{i,f} \varepsilon_{i,f} F_i^k \left(T_{k,abs}^4 - T_{i,abs,f}^4\right) A_k \end{aligned} \tag{4-c}$$

$$Q_{i,lat,f} = \varphi_{i,f} Q_{ik,lat} \tag{4-d}$$

where $H_{i,f}^{af}$ is the heat transfer coefficient between ambient air and node i in foliage layer; T_{af} is near-canopy air temperature for foliage layer; F is view factor, in which superscript is emitting surface and subscript is receiving surface; $\beta_{i,f}$ is foliage coverage ratio of surface for node i; $Q_{ik,\ lat}$ is latent heat generated from evapotranspiration for node i and k; other notations in Equation (4) and following equations can be found in the nomenclature.

3.1.3. Heat balance within soil

Similar to the heat balance of foliage, the heat transfer process within the soil can be expressed as:

$$\int_{V_{i,s}} \rho_s(x_i, y_i, z_i) c_{p,s}(x_i, y_i, z_i) dV_{i,s} \frac{dT_{i,s}}{dt}$$
$$= H_{i,s}^{as}(T_{as} - T_{i,s}) + H_{i,s}^{i-1}T_{i-1} + H_{i,s}^{i+1}T_{i+1} - \left(H_{i,s}^{i-1} + H_{i,s}^{i+1}\right)T_{i,s} + Q_{i,sw,s} + Q_{i,lw,s} + Q_{i,lat,s} \tag{5-a}$$

$$Q_{i,sw,s} = (1 - \beta_{i,f})\alpha_{i,s} I\downarrow_s A_{i,s} \tag{5-b}$$

$$Q_{i,lw,s} = \left[F_i^{sky}\left(T_{sky,abs}^4 - T_{i,abs,s}^4\right) + F_i^{grd}\left(T_{grd,abs}^4 - T_{i,abs,s}^4\right) + F_i^{air\_ex}\left(T_{air\_ex,abs}^4 - T_{i,abs,s}^4\right)\right] \cdot \sigma(1 - \beta_{i,f})\varepsilon_{i,s} A_{i,s} + \sum_k \sigma\theta_{i,s}\varepsilon_{i,s} F_i^k\left(T_{k,abs}^4 - T_{i,abs,s}^4\right)A_k \tag{5-c}$$

$$Q_{i,lat,s} = \varphi_{i,s} Q_{ik,lat} \tag{5-d}$$

where T_{as} is canopy air temperature near the soil layer; $\alpha_{i,s}$ is solar absorptivity.

3.1.4. Heat balance within the 3D-printed concrete wyeth

The heat transfer within the concrete wyeth in a 3D-VtGW module shown in Fig. 3 can be expressed as one of the three node types:

(1) Exterior surface node

$$\int_{V_{i,w}} \rho_w(x_i, y_i, z_i) c_{p,w}(x_i, y_i, z_i) dV_{i,w} \frac{dT_{i,\ w}}{dt}$$
$$= H_{i,w}^{aw}(T_{aw} - T_{i,\ w}) + H_{i,w}^{i-1}T_{i-1} + H_{i,w}^{i+1}T_{i+1} - \left(H_{i,w}^{i-1} + H_{i,w}^{i+1}\right)T_{i,w} + Q_{i,sw,w} + Q_{i,lw,w} \tag{6-a}$$

$$Q_{i,sw,w} = (1 - \beta_{i,f})\alpha_{i,w} I_s^{\downarrow} A_{i,w} \tag{6-b}$$

$$Q_{i,lw,w} = \left[F_i^{sky}\left(T_{sky,abs}^4 - T_{i,abs,w}^4\right) + F_i^{grd}\left(T_{grd,abs}^4 - T_{i,abs,w}^4\right) + F_i^{air\_ex}\left(T_{air\_ex,abs}^4 - T_{i,abs,w}^4\right)\right] \cdot \sigma(1 - \beta_{i,f})\varepsilon_{i,w} A_{i,w} + \sum_k \sigma\theta_{i,w}\varepsilon_{i,w} F_i^k\left(T_{k,abs}^4 - T_{i,abs,w}^4\right)A_k \tag{6-c}$$

where $H_{i,w}^j$ is heat transfer coefficient between air node j and wall node i; $F_i^k$is view factor for node i with exterior emitting surface k – i.e., wall or window and foliage surfaces.

(2) Internal node

$$\int_{V_{i,w}} \rho_{i,\ w}(x_i, y_i, z_i) c_{p,w}(x_i, y_i, z_i) dV_{i,w} \frac{dT_{i,\ w}}{dt}$$
$$= H_{i,w}^{i-1}T_{i-1} + H_{i,w}^{i+1}T_{i+1} - \left(H_{i,w}^{i-1} + H_{i,w}^{i+1}\right)T_{i,w} \tag{7}$$

(3) Interior surface node

Short-wave radiation from lighting ($Q_{i,sw}^{light}$), long-wave radiation from occupant activities, lighting and equipment ($Q_{i,lw}^{people}$, $Q_{i,lw}^{light}$, $Q_{i,lw}^{equip}$) applied on interior surfaces were considered.

$$\int_{V_{i,w}} \rho_{i,\ w}(x_i, y_i, z_i) c_{p,w}(x_i, y_i, z_i) dV_{i,w} \frac{dT_{i,\ w}}{dt}$$
$$= H_{i,w}^{j}(T_j - T_{i,\ w}) + H_{i,w}^{i-1}T_{i-1} + H_{i,w}^{i+1}T_{i+1} - \left(H_{i,w}^{i-1} + H_{i,w}^{i+1}\right)T_{i,w} + Q_{i,sw,w} + Q_{i,lw,w} \tag{8-a}$$

$$Q_{i,sw,w} = \alpha_{i,w} I_s^{\downarrow} A_{i,w} + Q_{i,sw}^{light} \tag{8-b}$$

$$Q_{i,lw,w} = \sum_k \sigma\theta_{i,w}\varepsilon_{i,w} F_i^k\left(T_{k,abs}^4 - T_{i,abs,w}^4\right)A_k + Q_{i,lw}^{people} + Q_{i,lw}^{light} + Q_{i,lw}^{equip} \tag{8-c}$$

3.1.5. Heat and moisture balance of canopy air

Heat balance of canopy air node j can be expressed as the following.

$$\rho_j c_{p,j} V_j \frac{dT_j}{dt} = H_j^{i,f}(T_{i,f} - T_j) + H_j^{i,s}(T_{i,s} - T_j) + H_j^{i,w}(T_{i,w} - T_j) + c_{p,j}\dot{m}_j^{air\_ex}(T_{air\_ex} - T_j) \tag{9}$$

where $H_j^{i,f}$ is heat transfer coefficient representing convection between canopy air node j and foliage node i.

The moisture balance of canopy air node j is expressed as:

$$\dot{W}_j = w_j^f + w_j^s + w_j^{air\_ex} \tag{10}$$

where W_j is water mass in the canopy air node j;w_j^f, w_j^s and $w_j^{air\_ex}$ are moisture transfer rate from foliage, soil and outdoor air, respectively.

3.1.6. Heat and moisture balance of indoor air

The heat transfer process for indoor air includes convective heat exchange with interior wall and window surfaces, air conditioning, infiltration and absorption of heat from internal gains $Q_{j,int}$ generated by occupant activity, $Q_{j,conv}^{people}$ lighting $Q_{j,conv}^{light}$, and equipment $Q_{j,conv}^{equip}$. The heat balance of indoor air node j is expressed as:

$$\rho_j c_{p,j} V_j \frac{dT_j}{dt} = \sum_k H_j^k(T_k - T_j) + c_{p,j}\dot{m}_j^{sys}(T_{sup,j} - T_j) + c_{p,j}\dot{m}_j^{inf}(T_{air\_ex} - T_j) + Q_{j,int} \tag{11-a}$$

$$Q_{j,int} = Q_{j,conv}^{people} + Q_{j,conv}^{light} + Q_{j,conv}^{equip} \tag{11-b}$$

where $\dot{m}_j^{sys}$ and $\dot{m}_j^{inf}$ are mass flow rate into indoor zone for air node j from air conditioner and outdoor air, respectively; $T_{sup,j}$ is the supply air temperature of air conditioner for indoor air node j.

The moisture balance for indoor air node j is:

$$\dot{W}_j = w_j^{int} + w_j^{sys} + w_j^{inf} \tag{12}$$

where W_j is water mass of indoor air node j, w_j^{int}, w_j^{sys} and w_j^{inf} are moisture transfer rate for indoor air node j from internal latent heat gains, air conditioning system supply air and infiltration.

3.1.7. Latent heat

Evapotranspiration is the combination of two different processes that occur simultaneously, evaporation from the soil surface or the wet vegetation and transpiration from the vegetation [42,43]. Over the past years, a number of empirical models have been developed to simulate the latent heat brought by the evapotranspiration process within the greenery system [38,42,44,45]. Among them, the Penman-Monteith equation originally developed for crops [42] has been widely adopted for the simulation of the evapotranspiration process for green walls and green roofs [37,41,43,46,47]. Studies by Ouldboukhitine et al. [48], Davis and Hirmer [49] pointed out that the FAO-56 Penman-Monteith equation tends to under predict the evapotranspiration in building greenery systems, whereas a number of experimental studies [37,46,47] have indicated that the generic format of Penman-Monteith equation is suitable for green walls/roofs after minor modifications based on plant species and irrigation condition etc.

[43,49,50]. In this study, the soil is assumed to be constantly irrigated for the simplicity of analysis and illustration.

The general form of Penman–Monteith equation can be written as [42]:

$$Q_{ik,lat} = \frac{\Delta(R_n - G) + \rho_a c_p (e_s - e)/r_a}{\Delta + \gamma(1 + r_s/r_a)} \tag{13}$$

where Δ is the slope of the saturation vapor pressure–temperature curve; G is heat absorbed by soil; ρ_a is air density; $c_{p,a}$ is the specific heat of air; γ is psychrometric constant; e_s is saturation vapor pressure of air, e is the actual vapor pressure; r_s is (bulk) surface resistance [42]:

$$r_s = \frac{r_l}{LAI_{active}} \tag{14}$$

where LAI_{active} is the active (sunlit) leaf area index [43]; and r_l is bulk stomatal resistance. R_n is net radiation at foliage surface [43]:

$$R_n = Q_{sw,f} - Q_{lw,f} \tag{15}$$

and r_a is aerodynamic resistance adopted from [43,50]:

$$r_a = \frac{100\sqrt{d/u}}{LAI_{active}} \tag{16}$$

where d is the leaf characteristic length and u is the air velocity [43].

3.2. Thermal comfort

Thermal comfort indices – i.e., the Predicted Mean Vote (PMV) and Predicted Percentage of Dissatisfied (PPD) based on Frager's model [51] were used to evaluate thermal comfort-time performance of building with 3D-VtGW. PMV predicts the mean value of the votes of a large group of people considering influence from indoor environment (humidity, air temperature and velocity, mean radiant temperature) and human metabolism, while PPD gives a quantitative prediction for the percentage of thermally dissatisfied occupants shown as the following function of PMV:

$$PPD = 100 - 95e^{-0.03353PMV^4 - 0.2179PMV^2} \tag{17}$$

The Long-term Percentage of Dissatisfied (LPD) reflects occupants' long-term thermal comfort [52] defined by the following equation:

$$LPD(p,\ PPD) = \frac{\sum_{n=1}^{N}\sum_{r=1}^{R}(p_{r,n}\cdot PPD_{r,n}\cdot \Delta t_n)}{\sum_{n=1}^{N}\sum_{r=1}^{R}(PPD_{r,n}\cdot \Delta t_n)} \tag{18}$$

where $p_{r,n}$ is the occupation rate at n^{th} time step for r^{th} zone; $PPD_{r,n}$ is the percentage of dissatisfied; Δt_n is time step duration. This normalized index gives an overall impression of the building thermal comfort performance for all the occupants over the whole time. Frager's model is used to calculate percentage of dissatisfied for LPD.

3.3. State-space representation and computation details

The whole building simulation model is the network through assembling of all the layer nodes and air nodes as shown in Fig. 4(b), based on heat and moisture balance equations. The state-space representation [53] of the thermal network can then be written as:

$$\tilde{C}\,\tilde{M}\,\dot{\vec{T}} = \tilde{H}\,\vec{T} + \vec{Q} \tag{19-a}$$

$$\tilde{C} = \begin{bmatrix} \tilde{C}_L & 0 \\ 0 & \tilde{C}_A \end{bmatrix};\ M^{\sim} = \begin{bmatrix} \tilde{M}_L & 0 \\ 0 & \tilde{M}_A \end{bmatrix};\ \vec{T} = \begin{bmatrix} \vec{T}_L \\ \vec{T}_A \end{bmatrix}$$
$$H^{\sim} = \begin{bmatrix} \tilde{H}_{LL} & \tilde{H}_{LA} \\ \tilde{H}_{AL} & \tilde{H}_{AA} \end{bmatrix};\ \vec{Q} = \begin{bmatrix} \vec{Q}_L \\ \vec{Q}_A \end{bmatrix} \tag{19-b}$$

The building's thermal behavior is solved by the discrete state space model through discretization of time:

$$\vec{T}_{n+1} = \left(E + \Delta t\tilde{C}^{-1}\tilde{M}^{-1}\tilde{H}\right)\vec{T}_n + \Delta t\tilde{C}^{-1}\tilde{M}^{-1}\vec{Q} \tag{20}$$

where $\tilde{C}$ is the thermal capacitance matrix; $\tilde{M}$ is the modification matrix for surface nodes; $\tilde{H}$ is the heat transfer matrix; E is identical matrix; $\vec{T}$ is the node temperature vector; $\vec{Q}$ is the rate of heat exchange for node from different sources. Subscript L refers to thermal nodes representing wall, window, foliage, and soil; subscript A refers to air nodes (zone air, canopy air).

In the heat balance equation, long-wave radiation is linearized using the same method performed in reference [54]. Simple glazing system model [55] was used for windows in this building model, in which window layer is no-mass layer. Infrared heat transfer through window and back out short-wave radiation from indoor space were also considered. Model in reference [55] was used for calculating internal gains from occupants, lighting, and equipment. For each time step, heat balance and moisture balance were computed separately; model variables (e.g., air relative humidity) and air conditioning control were updated based on information from last step.

4. Case study

To quantify thermal performance and energy saving potential of buildings built with the 3D-VtGW, energy analyses were performed on two commercial buildings with different envelopes: one with the 3D-VtGW and another with conventional aerated concrete block wall. The buildings selected for comparative study have the same roof, floor and fenestration (windows and door) materials. The window-to-wall ratio is 25% for the exterior envelopes. The building with 3D-VtGW was implemented with greenery on all four exterior walls (opaque portion of the vertical envelope); the baseline exterior wall was made of aerated concrete with the same overall R-value (1 K·m^2/W) as the 3D-VtGW. Both buildings were assumed to be used as small commercial buildings (i.e., cafeteria) with the dimension of 8.7 m (L) × 5.8 m (W) × 3.74 m (H). Automatic irrigation system was assumed to be installed on the top of each wall module, in conjunction with rain water harvest, to ensure proper water content in the soil. Other main simulation parameters include occupant activities, lighting, equipment and infiltration, which are enlisted in Fig. 5. It was also assumed that the long-wave absorptivity and long-wave emissivity are equal for both the soil and wall surfaces. CSWD of Nanjing, China were used for the simulation, Fig. 6 presents typical weather data during three representative seasons. Indoor temperature was controlled by air conditioner within 20.5–23.9℃ in summer and 21.1–24.9℃ in winter.

5. Simulation results and discussion

Whole building energy simulation and thermal comfort analysis were carried out using the hydro-thermal network model developed in Section 3 over a typical meteorological year. The simulation results indicated that 3D-VtGW system has substantial potential to improve both energy conservation and thermal comfort performance of buildings.

5.1. Thermal performance of 3D-VtGW

As is shown in Figs. 7 and 8, an evident difference can be observed for the thermal behaviors between the 3D-VtGW wall and the aerated concrete block wall baseline. Similar to the results

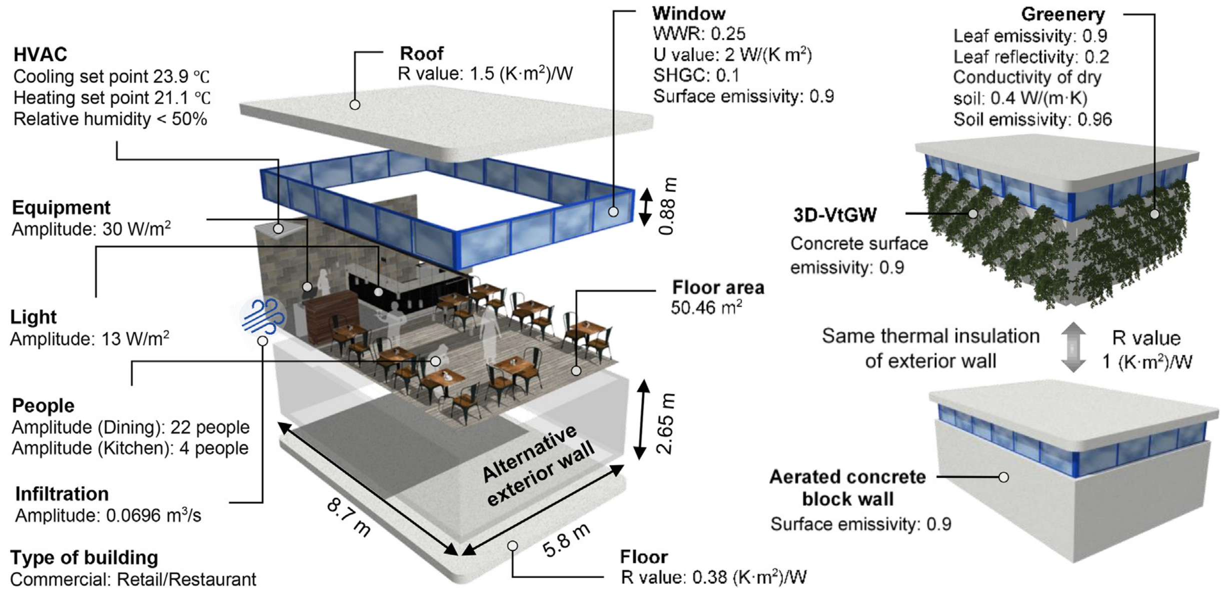

Fig. 5. Model parameters for the case study: buildings with 3D-VtGW vs. aerated concrete block wall.

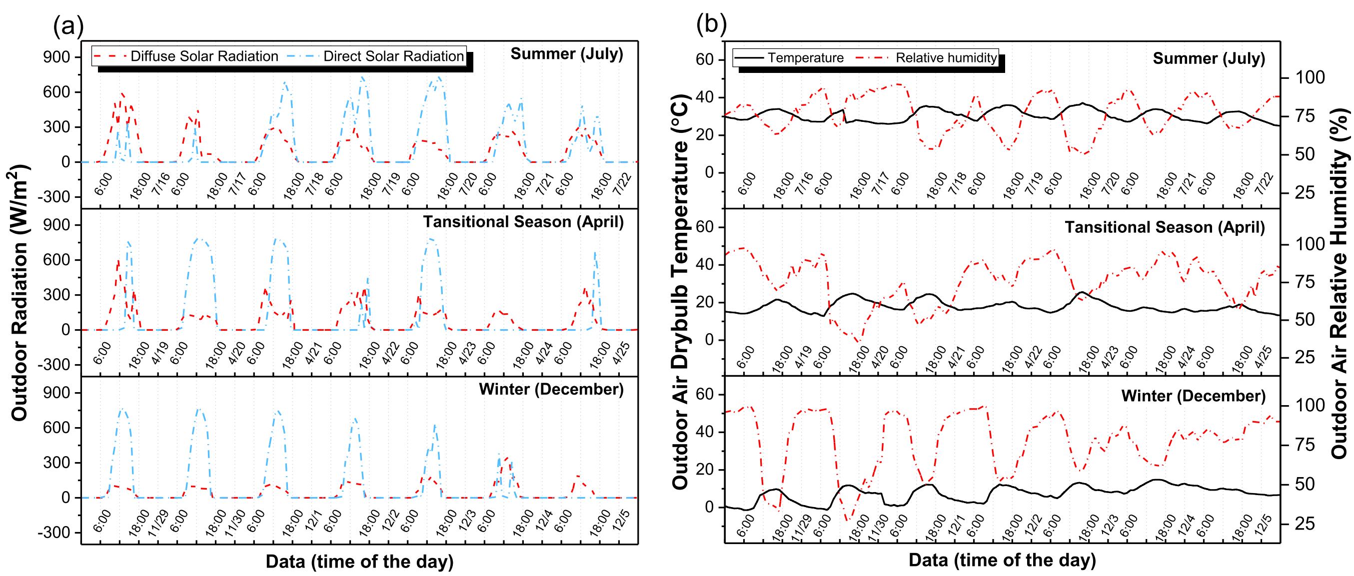

Fig. 6. Typical weather condition in Nanjing, China (extracted from CSWD).

from previous studies on green walls and green roofs [39], the exterior wall vertical surface temperature (weight average by area) of 3D-VtGW was notably lower in comparison with that of the baseline aerated concrete block wall. In summer, the maximum surface temperature of the aerated concrete wall baseline (west) reached over 60℃, whereas it remained only up to 35℃ for the 3D-VtGW during summer daytime as shown in Fig. 7. The west-facing wall is exposed to sunlight during afternoon hours and thus the temperature rises rapidly and reaches its peak value. The exterior surface temperature of 3D-VtGW also increases during day hours, but the peak temperature is significantly lower than that of the conventional wall – i.e., the rise of greenery system surface temperature is much more gradual. The vegetation together with wet soil protect building envelope from rapid temperature rise through evapotranspiration effects and solar shading similar to other VGS systems [39].

Apart from the benefits mentioned, 3D-VtGW also provides additional insulation (from plants and soil) to help maintaining indoor thermal environment. Under different weather conditions, VGS often shows notably different performances – i.e., generally living walls show a better thermal performance than common walls in summer than that during winter and transitional seasons [39]. Because of the combined effects of evaporative cooling, foliage shading, and heat storage of substrate soil, average surface temperature of the concrete support layer within 3D-VtGW showed delay and significant attenuation compared with that of the baseline aerated concrete wall, see Fig. 7. It was observed that even during the nights of hot summer days, the surface temperature of exterior concrete support layer of the 3D-VtGW is still below the surface temperature of aerated concrete block wall due to the evaporation promoted by hot exterior air temperature. During transitional seasons, the 3D-VtGW only shows cooling

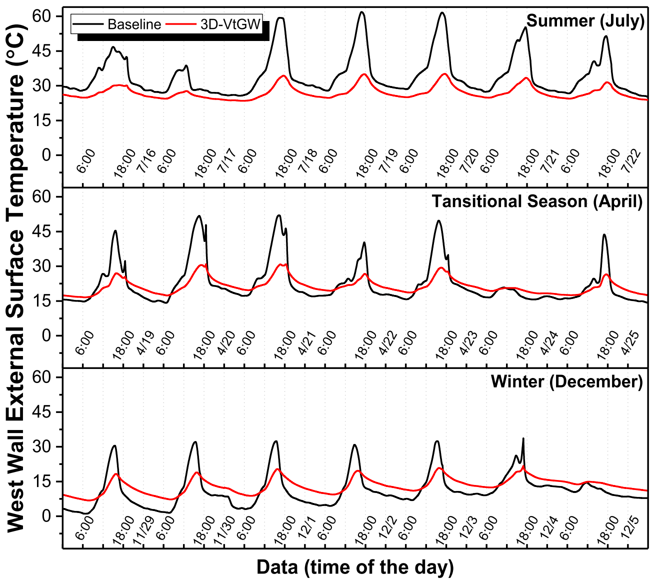

Fig. 7. Typical wall exterior surface temperature of 3D-VtGW and baseline.

effect during daytime. In winter, because the average indoor temperature is higher than average outdoor temperature, 3D-VtGW serves as heat sink in the daytime and resistance at night.

Fig. 8 shows the heat flux through each exterior wall. The results indicate that the 3D-VtGW system effectively reduces the peak heat flux through exterior wall, especially during summer daytime through high solar-induced evapotranspiration. Since orientation has a significant influence on the solar radiation acting on the building envelope, the heat flux through the west-facing wall is notably higher than the other walls. This orientation-dependent heat flux difference is particularly evident with the baseline aerated concrete block wall due to rapid exterior temperature rise as previously discussed. Whereas for 3D-VtGW, there is relatively small difference in through-wall heat flux of different orientations in both summer and winter, see Fig. 8. Relative heat flux reduction for 3D-VtGW compared with the baseline indicates that west wall brings largest thermal benefits in summer; and south 3D-VtGW wall exhibits most beneficial behavior as compared to baseline.

To investigate the cooling mechanism of the 3D-VtGW, an energy balance analysis was carried out using the simulation results. As shown in Fig. 9, the radiative, conductive, latent, convective energy flow and energy balance are obtained from the simulation results. It was found that on the foliage surface net solar radiation is the major heat gain in the daytime for both summer and winter months. Evapotranspiration dissipates most of heat gain on the foliage surface in summer. In winter, long-wave radiation and convection also contributes to the heat dissipation from the foliage. This observation is consistent with the findings from other studies on living walls [37] showing the influence of the outdoor environment via both the convective energy flow from canopy airflow and long-wave radiation exchanged with the outdoor environment. Fig. 9 (b) and (d) present the heat balance at the soil node for a typical summer and winter day, respectively. In summer, water evaporation from the soil layer would dissipate a large portion of the in-coming heat, further reducing the through-wall heat flux and fostering the passive cooling effect from greenery, see Fig. 9 (e). It is worth noting that this configuration with complex geometric features was enabled by concrete 3D printing technique with much lower construction cost as compared to conventional construction technique. Under the combined effect of evapotranspiration, vegetation shading and the thermal storage, the average heat flux transferred into the room through 3D-VtGW is 3.94 W/m^2 less than that through baseline aerated concrete block wall during summer months. During transitional seasons, the plant transpiration still provides effective cooling during the daytime, where the average through wall heat flux was also largely reduced. Stomatal resistance of plant increases in winter responding to lower outdoor temperature and solar radiation compared with that in summer [38], evaporation cooling effect from the greenery system is relatively small, whereas the greenery

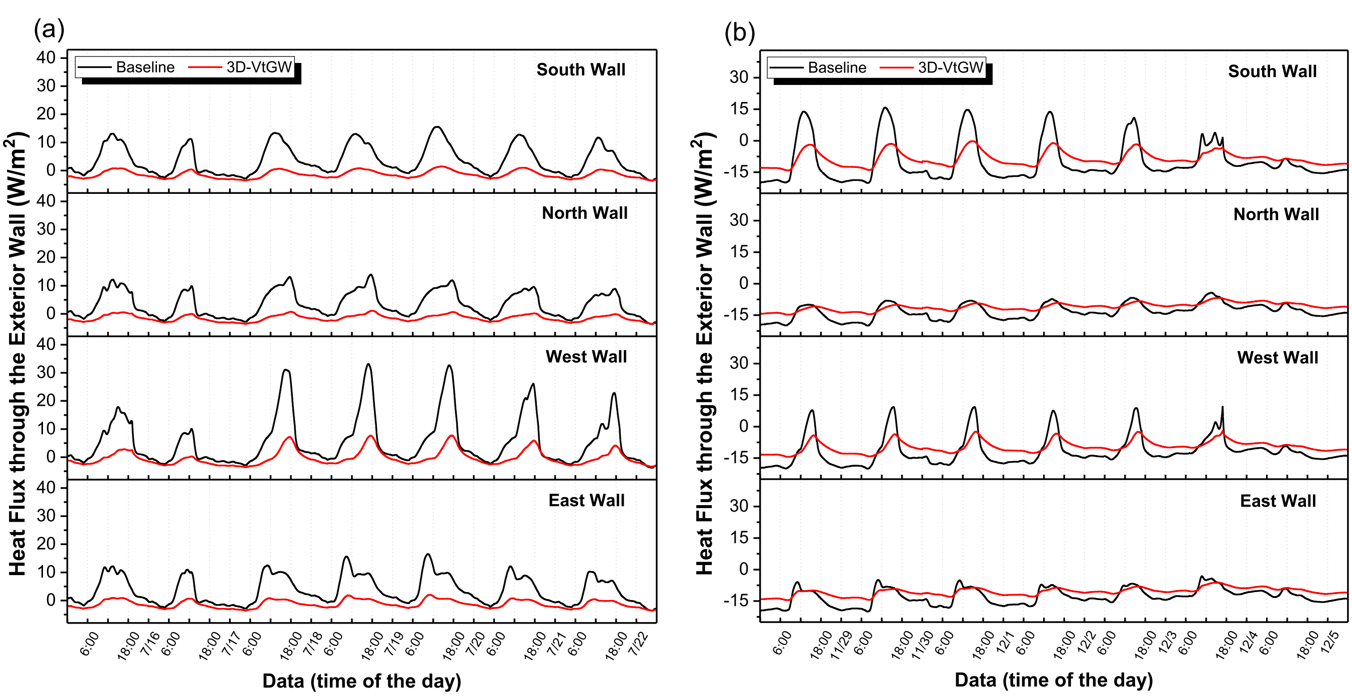

Fig. 8. Typical wall heat flux of 3D-VtGW and baseline in (a) summer (b) winter.

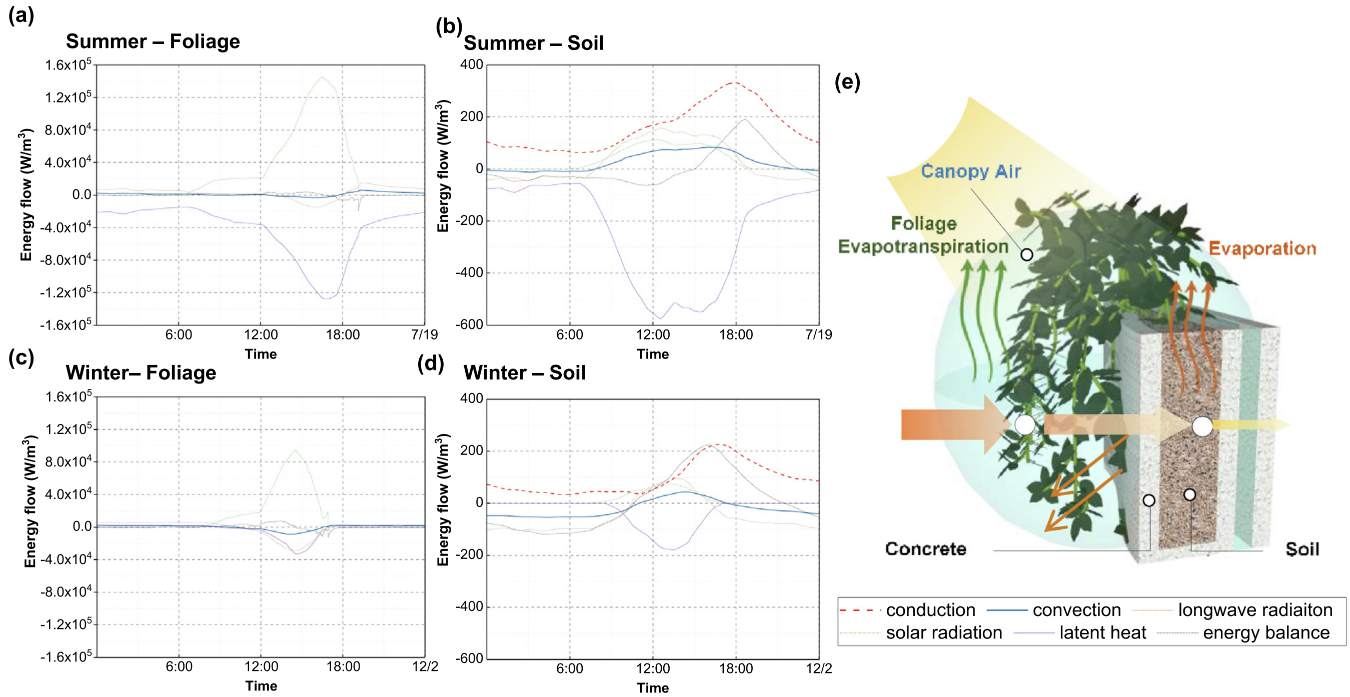

Fig. 9. Energy flow from different sources for a typical wall module in west 3D-VtGW exterior wall in summer.

serves as heat sink and reduces unbeneficial heat flux through exterior envelope by 2.88 W/m^2 compared with baseline.

5.2. Energy saving potential of 3D-VtGW

The monthly air conditioning (AC) load was obtained for the case study building with the 3D-VtGW. The AC load reduction is obtained by comparing to a reference building (same configuration) with the common aerated concrete block wall. Fig. 10 (a) presents comparison of the daily AC loads compared between the 3D-VtGW building and baseline building during two typical summer days in July. The AC load reduction ranges from 15% to 20% over typical summer days during the occupied hours with some fluctuations during the day. It is noted that the AC is scheduled off 1:00 am -5:00 am every day when the building is unoccupied. As a result, during warm summer nights the indoor air temperature of reference building may continuously rise during these hours, whereas the greenery system kept the indoor air temperature of 3D-VtGW building relatively cooler when AC is off. The AC load reduction is higher during afternoon hours due to the high evapotranspiration from the 3D-VtGW, which is consistent with the temperature and heat fluxes presented in the previous sections.

Fig. 10 (b) presents the monthly AC loads comparison (and reduction) for the case study building with 3D-VtGW and the aerated concrete block wall baseline. The simulation results show that the energy saving potential for the 3D-VtGW envelope is higher during summer months (May-August) than in transitional season and winter month, with maximum reduction occurs in June (12.00% cooling load reduction). It should be noted that the seemed higher percentage saving in winter months (November-February) than that in transitional seasons is mostly due to the relatively lower monthly energy use. The percentage of saving greatly depends upon external factors such as building type, building dimension, and environmental factors. When considering the monthly variation of energy saving it is consistent with the previous experimental study [38], which showed that when solar radiation is higher, living wall systems can provide higher energy saving – when a vertical greenery system receives higher solar radiation, the thermal benefits increases. Since the building studied herein is a cafeteria with high internal heat gains from occupants, lighting and equipment, thus, the winter month heating energy demand is lower than the cooling load demand in the summer.

5.3. Thermal comfort performance of 3D-VtGW

In order to evaluate the potential of 3D-VtGW to improve building's indoor thermal comfort, the Frager's model is adopted [51]. The predicted percentage of dissatisfied (PPD) index is obtained from the simulation results based on the formula given in Section 3. It is evident that the 3D-VtGW system reduces the predicted percentage of discomfort for all seasons. Fig. 11 (a) presents the PPD values for both buildings with 3D-VtGW and aerated concrete block wall during two typical summer days, where the PPD for the baseline building hovers round 25% throughout the operation hours. The higher PPD value occurs when the outside temperature or the occupation rate is high (during afternoon and evening hours). The building with 3D-VtGW shows similar trend, whereas the PPD values are lower than that of the baseline building with PPD remains under 20% for most of the operation hours. Fig. 11 (b) presents the monthly long-term percentage of dissatisfied (LPD) of the 3D-VtGW building as compared to the baseline building. Similar to the AC load reduction as shown in Fig. 10 (b), the thermal comfort improvement shows highest potential during summer months (May through September), with the annual LPD decreased by 10.20% (i.e., the Yearly LPD reduced from 12.26% for the baseline to 11.00% for the building with 3D-VtGW).

5.4. The effects of insulation

Apart from some other parameters impacting the behavior of greenery systems, such as LAI, surface reflectivity [37], exterior environment (solar radiation, relative humidity) [38], the thermal insulation of supporting layers adjacent to soil and foliage has a

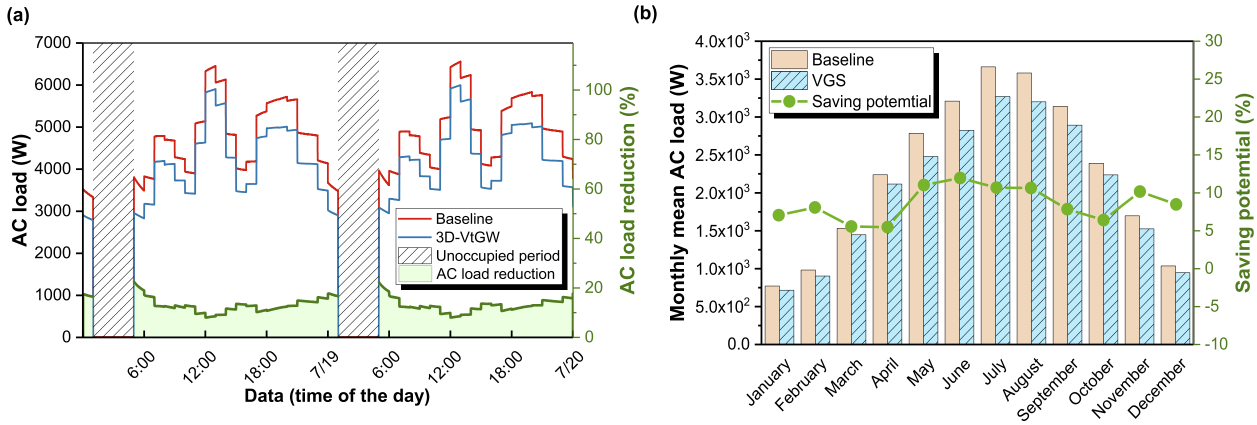

Fig. 10. AC load reduction of the building with 3D-VtGW and baseline: (a) AC load in summer days (b) Monthly mean AC load.

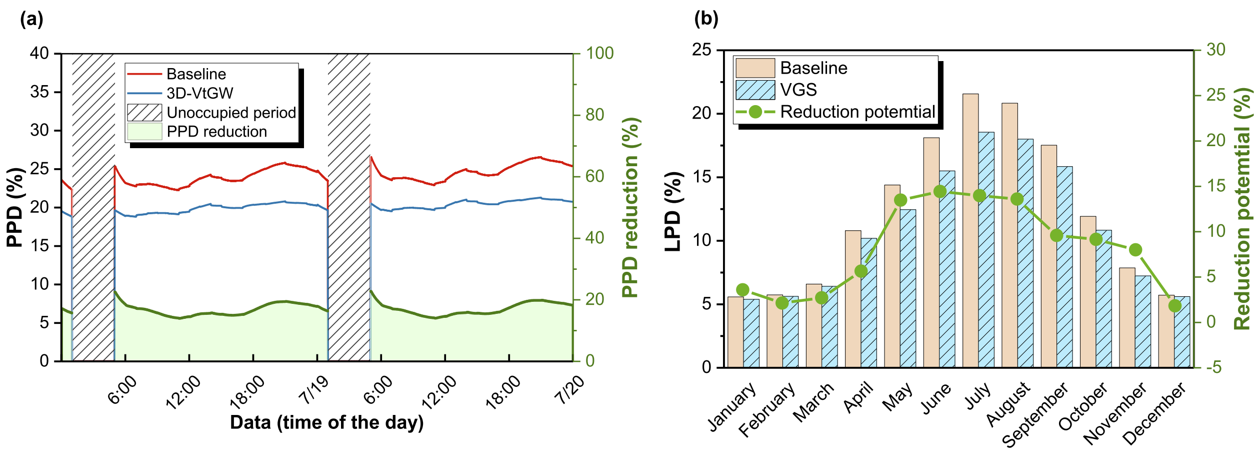

Fig. 11. Thermal comfort of building with 3D-VtGW and baseline: (a) PPD in summer days (b) Monthly LPD.

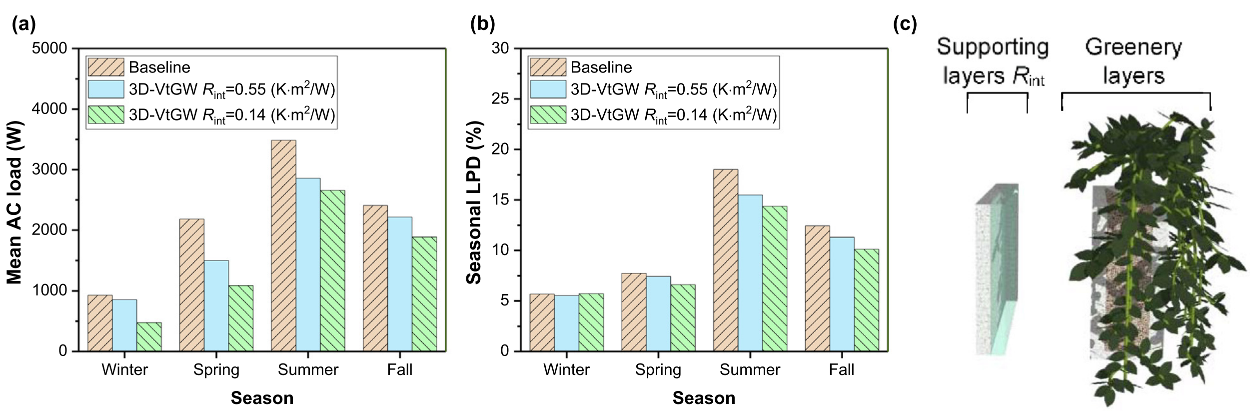

Fig. 12. Seasonal energy performance of 3D-VtGWs with different interior thermal insulation compared with baseline: (a) mean AC load under different conditions; (b) thermal comfort index, and (c) schematic showing R_{int}.

significant influence on the effectiveness of the 3D-VtGWs (i.e., AC load reduction and thermal comfort improvement are shown in Fig. 12 (b)). Fig. 12 (a) shows that under the internal gains level of a commercial building (high internal gain), 3D-VtGWs with low thermal insulation, R_{int}, as shown in Fig. 12 (c) brought higher AC load reduction in summer and transitional season as compared to 3D-VtGWs with higher thermal insulation levels. Even during winter months, lower insulation level also shows beneficial effect in terms of energy saving – i.e., the yearly AC load reduction ratio of 3D-VtGW with low thermal insulation R_{int} was 22.95%, which was much higher than 9.12% AC load reduction for 3D-VtGW with high thermal insulation R_{int}. This is mainly due to that lower level of insulation improves the utilization of greenery cooling effect by promoting heat conduction from the greenery layer to the hot indoor air. Similarly, improvements in thermal comfort was also observed for building with lower R_{int} during spring, summer and fall. Based on this observation, it is projected that the performance of living wall systems is dependent on both the environmental conditions, infiltration level, the level of internal gains (building type, occupancy conditions etc.), as well as the envelope insulation level. Therefore, it is speculated that living wall systems including 3D-VtGWs may show higher benefits with dynamic insulation [56,57] that can modulate insulation levels based on the demand.

6. Conclusions

Large-scale 3D printing has opened enormous opportunities for multifunctional building envelope design. In this research, a modular building envelope with integrated vertical greenery system, namely 3D printed Vertical Green Wall (3D-VtGW), was developed with the aid of concrete 3D printing technology. The 3D-VtGW was designed and produced using an integrated design-build (print) platform, enabling workflow for rapid customized design optimization, and prototyping of high-performance building envelops to satisfy multiple design requirements. The energy saving potential of a small commercial building assembled from 3D printed modular living wall system was demonstrated. A thermal nodal network model was formulated to calculate the thermal performance of buildings with 3D-printed heterogenous building envelope with vertical greenery system, with the consideration of both heat and moisture balance of the living wall components and air. Heat transfer process through the heterogenous living wall was captured by discretized state space equation.

Energy analyses of two archetype buildings were carried out as case studies: one with the 3D-VtGW and another baseline building with conventional aerated concrete block wall with similar thermal insulation level. The simulation results indicate that 3D-VtGW system exhibited excellent energy saving potential and improved thermal comfort. For the case-study archetype buildings (i.e., small commercial building) demonstration herein, the 3D printed green wall system largely reduces exterior wall surface temperature in summer as well as the heat flux through exterior walls. 3D-VtGW system brought 11.20% AC load reduction in summer and yearly 9.12% AC load reduction compared with baseline. The building with 3D-VtGW provided improved yearly thermal comfort, especially during summer and transitional season reducing LPD of baseline by 10.20%.

For buildings with high internal gain like the ones demonstrated in this study, lower insulation of exterior building envelope brought beneficial thermal behavior due to the promoted heat dissipation through the living wall. The observation leads to the belief that variable/dynamic insulation may enhance the performance of green wall systems, although the topic falls outside the scope of the current study. This research serves as a demonstration of the application of large-scale 3D printing to enable the construction of otherwise hard-to-produce or costly building components with complex geometry. The advancements in additive and subtractive manufacturing techniques and computational tools over the decade have opened pathways for producing building structures and components that were previously impossible or time-consuming to create. This largely expands the design space for high-performance building materials, components, and assemblies that have integrated functionalities such as structural, architectural (e.g., acoustic, thermal insulation, self-shading), and environmental functions (air quality melioration). Future research and developments are encouraged to explore these expanded spaces.

CRediT authorship contribution statement

Yawen He: Methodology, Software, Investigation, Writing - original draft. **Yamei Zhang:** Conceptualization, Funding acquisition, Resources. **Chao Zhang:** Visualization. **Hongyu Zhou:** Project administration, Conceptualization, Funding acquisition, Writing - review & editing.

Declaration of Competing Interest

The authors declare that they have no known competing financial interests or personal relationships that could have appeared to influence the work reported in this paper.

Acknowledgements

This research was made possible by the U.S. National Science Foundation (NSF CMMI-1663302) and the National Key R&D program of China (2017YFC0703700 and 2018YFC0705800). The authors also would specially like to thank Mr. Jin Li from Nanjing Green Institute for Intelligent Additive Manufacturing Co. Ltd for facilitating this project.

Appendix A. Supplementary data

Supplementary data to this article can be found online at https://doi.org/10.1016/j.enbuild.2020.110110.

References

[1] L. Reiter, T. Wangler, N. Roussel, R.J. Flatt, The role of early age structural build-up in digital fabrication with concrete, Cem. Concr. Res. 112 (2018) 86–95, https://doi.org/10.1016/j.cemconres.2018.05.011.
[2] T.D. Ngo, A. Kashani, G. Imbalzano, K.T.Q. Nguyen, D. Hui, Additive manufacturing (3D printing): a review of materials, methods, applications and challenges, Compos. Part B Eng. 143 (2018) 172–196, https://doi.org/10.1016/j.compositesb.2018.02.012.
[3] Y.W.D. Tay, B. Panda, S.C. Paul, N.A. Noor Mohamed, M.J. Tan, K.F. Leong, 3D printing trends in building and construction industry: a review, Virtual Phys. Prototyp. 12 (2017) 261–276, https://doi.org/10.1080/17452759.2017.1326724.
[4] I. Perkins, M. Skitmore, Three-dimensional printing in the construction industry: a review, Int. J. Constr. Manag. 15 (2015) 1–9, https://doi.org/10.1080/15623599.2015.1012136.
[5] G. De Schutter, K. Lesage, V. Mechtcherine, V.N. Nerella, G. Habert, I. Agusti-Juan, Vision of 3D printing with concrete — technical, economic and environmental potentials, Cem. Concr. Res. 112 (2018) 25–36, https://doi.org/10.1016/j.cemconres.2018.06.001.
[6] R.J.M. Wolfs, F.P. Bos, T.A.M. Salet, Early age mechanical behaviour of 3D printed concrete: Numerical modelling and experimental testing, Cem. Concr. Res. 106 (2018) 103–116, https://doi.org/10.1016/j.cemconres.2018.02.001.
[7] Scott Z. Jones, Dale P. Bentz NSM, William L. George and AT. Rheological Control of 3D Printable Cement Paste and Mortars. First RILEM Int. Conf. Concr. Digit. Fabr. – Digit. Concr. 2018, Springer; 2019, p. 70–80. doi: 10.1007/978-3-319-99519-9_31.
[8] S. Al-Qutaifi, A. Nazari, A. Bagheri, Mechanical properties of layered geopolymer structures applicable in concrete 3D-printing, Constr. Build. Mater. 176 (2018) 690–699, https://doi.org/10.1016/j.conbuildmat.2018.04.195.
[9] T.T. Le, S.A. Austin, S. Lim, R.A. Buswell, A.G.F. Gibb, T. Thorpe, Mix design and fresh properties for high-performance printing concrete, Mater. Struct. Constr. 45 (2012) 1221–1232, https://doi.org/10.1617/s11527-012-9828-z.
[10] Z. Liu, M. Li, Y. Weng, T.N. Wong, M.J. Tan, Mixture Design Approach to optimize the rheological properties of the material used in 3D cementitious material printing, Constr. Build. Mater. 198 (2019) 245–255, https://doi.org/10.1016/j.conbuildmat.2018.11.252.
[11] G. Ma, L. Wang, A critical review of preparation design and workability measurement of concrete material for largescale 3D printing, Front. Struct. Civ. Eng. 12 (2018) 382–400, https://doi.org/10.1007/s11709-017-0430-x.
[12] D. Asprone, C. Menna, F.P. Bos, T.A.M. Salet, J. Mata-Falcón, W. Kaufmann, Rethinking reinforcement for digital fabrication with concrete, Cem. Concr. Res. 112 (2018) 111–121, https://doi.org/10.1016/j.cemconres.2018.05.020.
[13] B. Nematollahi, M. Xia, J. Sanjayan, Current progress of 3D concrete printing technologies. ISARC 2017 – Proc 34th Int Symp Autom Robot Constr 2017:260–7. doi: 10.22260/isarc2017/0035.
[14] S. Lim, R. Buswell, T. Le, R. Wackrow, S. Austin, A. Gibb TT. Development of a viable concrete printing process. Proc. 28th Int. Symp. Autom. Robot. Constr., 2011, p. 665–670.
[15] R. Duballet, O. Baverel, J. Dirrenberger, Classification of building systems for concrete 3D printing, Autom. Constr. 83 (2017) 247–258, https://doi.org/10.1016/j.autcon.2017.08.018.

[16] E. Barnett, C. Gosselin, Large-scale 3D printing with a cable-suspended robot, Addit. Manuf. 7 (2015) 27–44, https://doi.org/10.1016/j.addma.2015.05.001.
[17] B. Mazhoud, A. Perrot, V. Picandet, D. Rangeard, E. Courteille, Underwater 3D printing of cement-based mortar, Constr. Build. Mater. 214 (2019) 458–467, https://doi.org/10.1016/j.conbuildmat.2019.04.134.
[18] N. Leach, E. Dini, F. Partners, 3D printing in space, Archit. Des. 86 (2014) 108–113.
[19] F. Bos, R. Wolfs, Z. Ahmed, T. Salet, Additive manufacturing of concrete in construction: potentials and challenges of 3D concrete printing, Virtual Phys. Prototyp. 11 (2016) 209–225, https://doi.org/10.1080/17452759.2016.1209867.
[20] C. Gosselin, R. Duballet, P. Roux, N. Gaudillière, J. Dirrenberger, P. Morel, Large-scale 3D printing of ultra-high performance concrete – a new processing route for architects and builders, Mater. Des. 100 (2016) 102–109, https://doi.org/10.1016/j.matdes.2016.03.097.
[21] K. Biswas, J. Rose, L. Eikevik, M. Guerguis, P. Enquist, B. Lee, et al., Additive manufacturing integrated energy-enabling innovative solutions for buildings of the future, J. Sol. Energy Eng. Trans. ASME (2017) 139, https://doi.org/10.1115/1.4034980.
[22] I. Wawrek, Zero house by 3D printer technology. IOP Conf Ser Mater Sci Eng 2019, 566. doi: 10.1088/1757-899X/566/1/012037.
[23] S. Yang, S. Wi, J.H. Park, H.M. Cho, S. Kim, Novel proposal to overcome insulation limitations due to nonlinear structures using 3D printing: hybrid heat-storage system, Energy Build. 197 (2019) 177–187, https://doi.org/10.1016/j.enbuild.2019.05.048.
[24] M.S. Khan, F. Sanchez, H. Zhou, 3-D printing of concrete: beyond horizons, Cem. Concr. Res. 133 (2020), https://doi.org/10.1016/j.cemconres.2020.106070 106070.
[25] M. Shafique, R. Kim, M. Rafiq, Green roof benefits, opportunities and challenges – a review, Renew. Sustain. Energy Rev. 90 (2018) 757–773, https://doi.org/10.1016/j.rser.2018.04.006.
[26] H.F. Castleton, V. Stovin, S.B.M. Beck, J.B. Davison, Green roofs; Building energy savings and the potential for retrofit, Energy Build. 42 (2010) 1582–1591, https://doi.org/10.1016/j.enbuild.2010.05.004.
[27] K. Vijayaraghavan, Green roofs: a critical review on the role of components, benefits, limitations and trends, Renew. Sustain. Energy Rev. 57 (2016) 740–752, https://doi.org/10.1016/j.rser.2015.12.119.
[28] G. Pérez, L. Rincón, A. Vila, J.M. González, L.F. Cabeza, Green vertical systems for buildings as passive systems for energy savings, Appl. Energy 88 (2011) 4854–4859, https://doi.org/10.1016/j.apenergy.2011.06.032.
[29] M. Manso, J. Castro-Gomes, Green wall systems: a review of their characteristics, Renew. Sustain. Energy Rev. 41 (2015) 863–871, https://doi.org/10.1016/j.rser.2014.07.203.
[30] C.Y. Jim, Greenwall classification and critical design-management assessments, Ecol. Eng. 77 (2015) 348–362, https://doi.org/10.1016/j.ecoleng.2015.01.021.
[31] L. Zhang, Z. Deng, L. Liang, Y. Zhang, Q. Meng, J. Wang, et al., Thermal behavior of a vertical green facade and its impact on the indoor and outdoor thermal environment, Energy Build. (2019) 204, https://doi.org/10.1016/j.enbuild.2019.109502.
[32] R. Jagarajan, M.N. Abdullah Mohd Asmoni, A.H. Mohammed, M.N. Jaafar, J. Lee Yim Mei, M. Baba, Green retrofitting – a review of current status, implementations and challenges, Renew. Sustain. Energy Rev. 67 (2017) 1360–1368, https://doi.org/10.1016/j.rser.2016.09.091.
[33] R. Castiglia Feitosa, S.J. Wilkinson, Attenuating heat stress through green roof and green wall retrofit, Build. Environ. 140 (2018) 11–22, https://doi.org/10.1016/j.buildenv.2018.05.034.
[34] H. Feng, K. Hewage, Lifecycle assessment of living walls: air purification and energy performance, J. Clean. Prod. 69 (2014) 91–99, https://doi.org/10.1016/j.jclepro.2014.01.041.
[35] M.R. Ismail, Quiet environment: acoustics of vertical green wall systems of the Islamic urban form, Front. Archit. Res. 2 (2013) 162–177, https://doi.org/10.1016/j.foar.2013.02.002.
[36] E. Alexandri, P. Jones, Temperature decreases in an urban canyon due to green walls and green roofs in diverse climates, Build. Environ. 43 (2008) 480–493, https://doi.org/10.1016/j.buildenv.2006.10.055.
[37] L. Malys, M. Musy, C. Inard, A hydrothermal model to assess the impact of green walls on urban microclimate and building energy consumption, Build. Environ. 73 (2014) 187–197, https://doi.org/10.1016/j.buildenv.2013.12.012.
[38] Y. He, H. Yu, A. Ozaki, N. Dong, S. Zheng, An investigation on the thermal and energy performance of living wall system in Shanghai area, Energy Build. 140 (2017) 324–335, https://doi.org/10.1016/j.enbuild.2016.12.083.
[39] K.C. Dahanayake, C.L. Chow, Comparing reduction of building cooling load through green roofs and green walls by EnergyPlus simulations, Build. Simul. 11 (2018) 421–434, https://doi.org/10.1007/s12273-017-0415-7.
[40] Theodore L. Bergman, Frank P. Incropera, David P. DeWitt ASL. Fundamentals of heat and mass transfer. Seventh Ed. John Wiley & Sons, Inc.; 2011.
[41] K.W.D.K.C. Dahanayake, C.L. Chow, Studying the potential of energy saving through vertical greenery systems: using EnergyPlus simulation program, Energy Build. 138 (2017) 47–59, https://doi.org/10.1016/j.enbuild.2016.12.002.
[42] R.G. Allen, L.S. Pereira, D. Raes, M. Smith, Crop evapotranspiration-Guidelines for computing crop water requirements FAO Irrigation and drainage paper 56. Food Agric Organ United Nations, Rome 1998.
[43] S. Flores Larsen, C. Filippín, G. Lesino, Modeling double skin green façades with traditional thermal simulation software, Sol. Energy 121 (2015) 56–67, https://doi.org/10.1016/j.solener.2015.08.033.
[44] D.J. Sailor, A green roof model for building energy simulation programs, Energy Build. 40 (2008) 1466–1478, https://doi.org/10.1016/j.enbuild.2008.02.001.
[45] P.C. Tabares-Velasco, J. Srebric, A heat transfer model for assessment of plant based roofing systems in summer conditions, Build. Environ. 49 (2012) 310–323, https://doi.org/10.1016/j.buildenv.2011.07.019.
[46] M. Scarpa, U. Mazzali, F. Peron, Modeling the energy performance of living walls: validation against field measurements in temperate climate, Energy Build. 79 (2014) 155–163, https://doi.org/10.1016/j.enbuild.2014.04.014.
[47] W.J. Stec, A.H.C. Van Paassen, A. Maziarz, Modelling the double skin façade with plants, Energy Build. 37 (2005) 419–427, https://doi.org/10.1016/j.enbuild.2004.08.008.
[48] S.E. Ouldboukhitine, R. Belarbi, R. Djedjig, Characterization of green roof components: measurements of thermal and hydrological properties, Build. Environ. 56 (2012) 78–85, https://doi.org/10.1016/j.buildenv.2012.02.024.
[49] M.M. Davis, S. Hirmer, The potential for vertical gardens as evaporative coolers: an adaptation of the "Penman Monteith Equation", Build. Environ. 92 (2015) 135–141, https://doi.org/10.1016/j.buildenv.2015.03.033.
[50] G. Bonan, Ecological climatology Concepts and Applications. second ed. Cambridge University Press; 2008.
[51] ISO. ISO 7730: Ergonomics of the thermal environment Analytical determination and interpretation of thermal comfort using calculation of the PMV and PPD indices and local thermal comfort criteria. Management 2005;3:605–15. doi: 10.1016/j.soildyn.2004.11.005.
[52] S. Carlucci, Thermal Comfort Assessment of Buildings. Springer Milan Heidelberg New York Dordrecht London; 2013. doi: 10.1007/978-88-470-5238-3.
[53] D. Kim, J.E. Braun, A general approach for generating reduced-order models for large multi-zone buildings, J. Build. Perform. Simul. 8 (2015) 435–448, https://doi.org/10.1080/19401493.2014.977952.
[54] J.W. Deardorff, Efficient prediction of ground surface temperature and moisture, with inclusion of a layer of vegetation, J. Geophys. Res. 83 (1978) 1889, https://doi.org/10.1029/jc083ic04p01889.
[55] L. Berkeley, O.A.K. Ridge, M.B.Y. Ut-battelle, A. For, S. Energy, D. Or, et al. EnergyPlusTM Version 8.9.0 Documentation Engineering Reference. 2019.
[56] V. Shekar, M. Krarti, Control strategies for dynamic insulation materials applied to commercial buildings, Energy Build. 154 (2017) 305–320, https://doi.org/10.1016/j.enbuild.2017.08.084.
[57] Q. Jin, F. Favoino, M. Overend, Design and control optimisation of adaptive insulation systems for office buildings. Part 2: A parametric study for a temperate climate, Energy 127 (2017) 634–649, https://doi.org/10.1016/j.energy.2017.03.096.